CONDENSED MATTER PHYSICS

Discovery of electric devil's staircase in perovskite antiferroelectric

Zhenqin Li[1,2]†, Zhengqian Fu[1]*†, Henghui Cai[2,3], Tengfei Hu[1,4], Ziyi Yu[1,4], Yue Luo[2,3], Linlin Zhang[1], Heliang Yao[1], Xuefeng Chen[3]*, Shujun Zhang[5], Genshui Wang[1,3], Xianlin Dong[1,3,4], Fangfang Xu[1,4]*

The devil's staircase, describing step-like function for two competing frequencies, is well known over a wide range of dynamic systems including Huyghens' clocks, Josephson junction, and chemical reaction. In condensed matter physics, the devil's staircase has been observed in spatially modulated structures, such as magnetic ordering. It draws widespread attentions because it plays a crucial role in the fascinating phenomena including phase-locking behaviors, commensurate-incommensurate phase transition, and spin-valve effect. Here, we report the observation of polymorphic phase transitions consisting of several steps in $PbZrO_3$-based system—namely, electric devil's staircase—originated from competing ferroelectric and antiferroelectric interactions. We fully characterize a specific electric dipole configuration by decomposing this competitive interaction in terms of basic structure and modulation function. Of particular interest is that the occurrence of many degenerate electric dipole configurations in devil's staircase enables superior energy storage performance. These observations are of great significance for exploring more substantive magnetic-electric correspondence and engineering practical high-power antiferroelectric capacitors.

INTRODUCTION

Both ferromagnetic and ferroelectric (FE) materials, arising from directional symmetry breaking during phase transition, can exhibit domain structures and the resulting hysteresis phenomenon under conjugated external fields. This unique and well-known analogy between the two ferroic systems provides a lasting impetus for the exploring one-to-one correspondence between the physical characteristics of magnetic and electric dipoles. The inspiring works have been recently reported including polar topological structures in $PbTiO_3/SrTiO_3$ superlattice (*1*, *2*), helical ordering in quadruple perovskite $BiCu_xMn_{7-x}O_{12}$ (*3*), noncollinear ferrielectricity (*4*), and electric Dzyaloshinskii-Moriya interaction (*5*).

The devil's staircase (DS) is of particular interest in condensed matter physics because it describes phase-locking behavior of competing interactions in a step-like fashion (*6*–*8*). Meanwhile, the DS behavior also plays a crucial role in the material's macroscopic properties, e.g., degenerate magnetic configurations mediated giant magnetoresistance in single-phase $SrCo_6O_{11}$ (*6*). The most famous phenomenon of this kind is magnetic DS of CeSb, which exhibits sequential appearance of six spin modulations with decreasing temperature below the Néel temperature (*9*–*14*). These modulated spin orderings comprise stacking of Ising-like ferromagnetic inserted with/without paramagnetic layers, establishing several antiferroparamagnetic and ground-state antiferromagnetic phases. In contrast, the DS of electric dipoles is rarely observed.

Because the DS always involves long-periodic modulated structures, antiferroelectric (AFE) perovskite oxides provide a potential opportunity for exploring the electric DS. Specifically, we start from $(Pb_{0.97}La_{0.02})(Zr_{0.50}Sn_{0.50})O_3$ (PLZS) AFE ceramic since our previous work has found that (i) its modulated structure is easily tunable by chemical substitution and (ii) it has nearly the same modulated period with prototypical $PbZrO_3$ at room temperature (*15*, *16*). In this work, we demonstrate temperature-driven electric DS, which involves three phase-locking steps with a large number of degenerate electric dipole configurations. Of particular importance is that the DS behavior of PLZS contributes to an ultrahigh energy storage density with good thermal stability over a broad temperature range.

RESULTS AND DISCUSSION

Figure 1A shows dielectric constant of PLZS ceramic as a function of temperature over the temperature range of −120° to 350°C. The temperature-dependent dielectric response can be divided into three regions, i.e., X, Y, and Z, exhibiting the increased, plateau-like, and decreased dielectric constants, respectively. On the basis of earlier works (*17*–*19*), region Y and region Z can be described as multicell and simple-cell cubic phases. The PLZS ceramic exhibits intriguing phase transitions in region X, which can be further divided into subregions X_1 to X_5 according to the varying slope of dielectric spectrum (also see fig. S1). The dielectric constants in neighboring subregions show gentle rather than abrupt variation, implying that only AFE phases exist in region X, because FE phase has significantly higher dielectric constant than AFE phase. These phase transitions resemble to polymorphic phase transition (PPT) in classic FE, for example, tetragonal to orthorhombic and then to rhombohedral phase transitions in $BaTiO_3$ (*20*). However, the notable difference is that PPT is diffused between AFE, while it is sharp between FE.

The unipolar polarization-electric field (*P*-*E*) hysteresis loops for each subregion (X_1 to X_5) are inserted in Fig. 1A. It can be seen that the polarization response changes from double loops (X_1) to multiple

[1]State Key Laboratory of High Performance Ceramics and Superfine Microstructures, Shanghai Institute of Ceramics, Chinese Academy of Sciences, Shanghai 200050, China. [2]University of Chinese Academy of Sciences, Beijing 100049, China. [3]The Key Lab of Inorganic Functional Materials and Devices, Shanghai Institute of Ceramics, Chinese Academy of Sciences, Shanghai 200050, China. [4]School of Physical Science and Technology, ShanghaiTech University, Shanghai 201210, China. [5]Institute for Superconducting and Electronic Materials, Australian Institute of Innovative Materials, University of Wollongong, Wollongong, New South Wales 2500, Australia.
*Corresponding author. Email: fmail600@mail.sic.ac.cn (Z.F.); xfchen@mail.sic.ac.cn (X.C.); ffxu@mail.sic.ac.cn (F.X.)
†These authors contributed equally to this work.

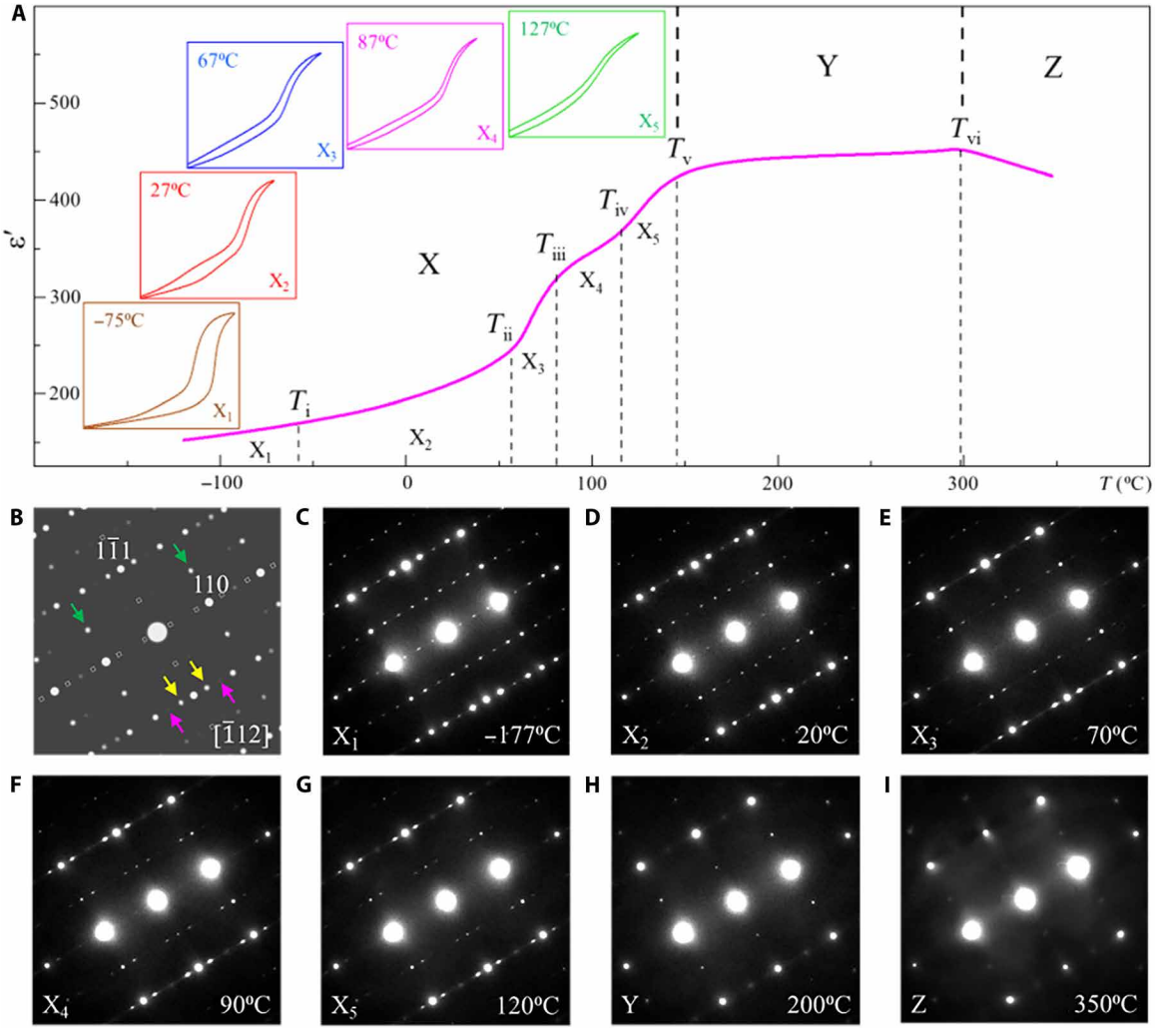

Fig. 1. Temperature-induced phase transition process in PLZS. (**A**) Temperature dependence of dielectric properties measured at 1 kHz. The characteristic temperatures are determined to be (see fig. S1) $T_i = -60$°C, $T_{ii} = 56$°C, $T_{iii} = 80$°C, $T_{iv} = 115$°C, $T_v = 146$°C, and $T_{vi} = 298$°C. The insets are the unipolar *P-E* loops for each subregion in X. All *P-E* loops have the same horizontal ($P = 0$ to 45 μC/cm^2) and vertical ($E = 0$ to 360 kV/cm) scale. (**B** to **I**) The simulated and experimental [1̄12]-projected SAED patterns in heating process. The 1/2{*ooo*}-type, 1/2{*ooe*}-type, and satellite reflections are marked by green, purple, and yellow arrows, respectively. The "*o*" and "*e*" refer to odd and even indices, respectively.

loops (X_2) and again back to double loops (X_3 to X_5) with increasing temperature. These features again confirm that the PPT in region X only involves AFE phases. The low-temperature double loops differ from high-temperature double loops in hysteresis extent (square versus slim), which is closely associated with their strong and weak first-order characters of AFE-FE phase transitions, respectively. The double to multiple and then to double loop behavior can be ascribed to phase transition between different modulated structures, on the basis of composition-induced *P-E* loop evolution (*16*).

To understand the phase transition sequence microscopically in PLZS, in situ selected-area electron diffraction (SAED) was carried out. The [1̄12] zone axis was chosen since it can simultaneously confirm three different types of structural distortion, i.e., satellite reflection is associated with atomic displacement modulation, 1/2{*ooo*}-type superlattice reflection is originated from antiphase oxygen octahedral tilting, and 1/2{*ooe*}-type superlattice reflection is induced by in-phase oxygen octahedral tilting in cubic phases (*17*, *21*, *22*). These superlattice reflections are marked by colored arrows in simulated SAED patterns of $PbZrO_3$ (Fig. 1B). The experimental SAED patterns in each region are presented in Fig. 1 (C to I), where three different stages can also be distinguished. That is, the regions X, Y, and Z in Fig. 1A are characterized by both satellites and 1/2{*ooo*}-type reflections (Fig. 1, C to G), sharp 1/2{*ooo*}-type and diffuse 1/2{*ooe*}-type reflections (Fig. 1H), and diffuse 1/2{*ooo*}-type and diffuse 1/2{*ooe*}-type reflections (Fig. 1I), respectively. These characteristic reflections confirm that regions X, Y, and Z are AFE, multicell cubic phase, and simple-cell cubic phase, respectively. To further examine the structural distortion for 1/2{*ooe*}-type reflections, SAED patterns along the [1$\bar{1}$0] zones are checked (fig. S2). The 1/2{*ooe*}-type reflections are forbidden in <110> zone axes since the *h* not equal to *k* applies for in-phase tilting. Thus, the appearance of 1/2{*ooe*} in fig. S2A and the absence of 1/2{*ooe*} in fig. S2 (B and C) indicate that these reflections are indeed resulted from in-phase tilt for cubic phases (*23*, *24*). The diffuse superlattice

reflections at the high temperature (Fig. 1I) indicate that the simple-cell cubic phase is in a short-range order of anti/in-phase tilting state, suggesting that the transition from simple-cell to multicell cubic phase did not occur directly from the *m*3*m* symmetry. In addition, distinct sharpening of the 1/2{*ooo*}-type reflections was observed in multicell cubic phase, manifesting that the antiphase tilting is dominant in the competition between antiphase and in-phase tilting and undergoes a noticeable increase in their degree of long-range order.

Of particular interest is that the PPT among AFE phases in region X is represented as the change of modulation wave vector (**q**), which is evidenced by the distance between satellite and basic reflections (Fig. 1, C to G). The fact that subregions X_1 and X_2 have the same modulation period wave vector (**q** = 1/4) but different hysteresis loops (double versus multiple) reveals that PLZS exhibits stable ground AFE state at low temperature rather than room temperature. Similar scenario was also observed in CeSb, in which two antiferroparamagnetic states transform without a clear change of the **q** value (*25*).

The observed temperature-induced variation of modulation wave vector from ground AFE state suggests the DS may occur in region X. Thus, we performed a more elaborate in situ observations in the heating process. Figure 2A shows the position of (**q** + 1, **q** − 1, 0) satellite reflection at increasing temperatures with horizontal alignment of the ($\bar{1}$10) basic reflection (also see fig. S3). It can be found that the PPTs among AFE phases exhibit two interesting behaviors. First, the distance between satellite and main reflection keeps unchanged and thus has a constant modulation wave vector within each subregion, i.e., **q** ≈ 1/4 for X_1 and X_2, **q** ≈ 2/9 for X_3, and **q** ≈ 1/5 for X_4. It should be noted that X_1 and X_2 can be equally treated in terms of structural phase transition although subregions have different physical natures. On the contrary, the **q** jumps, rather

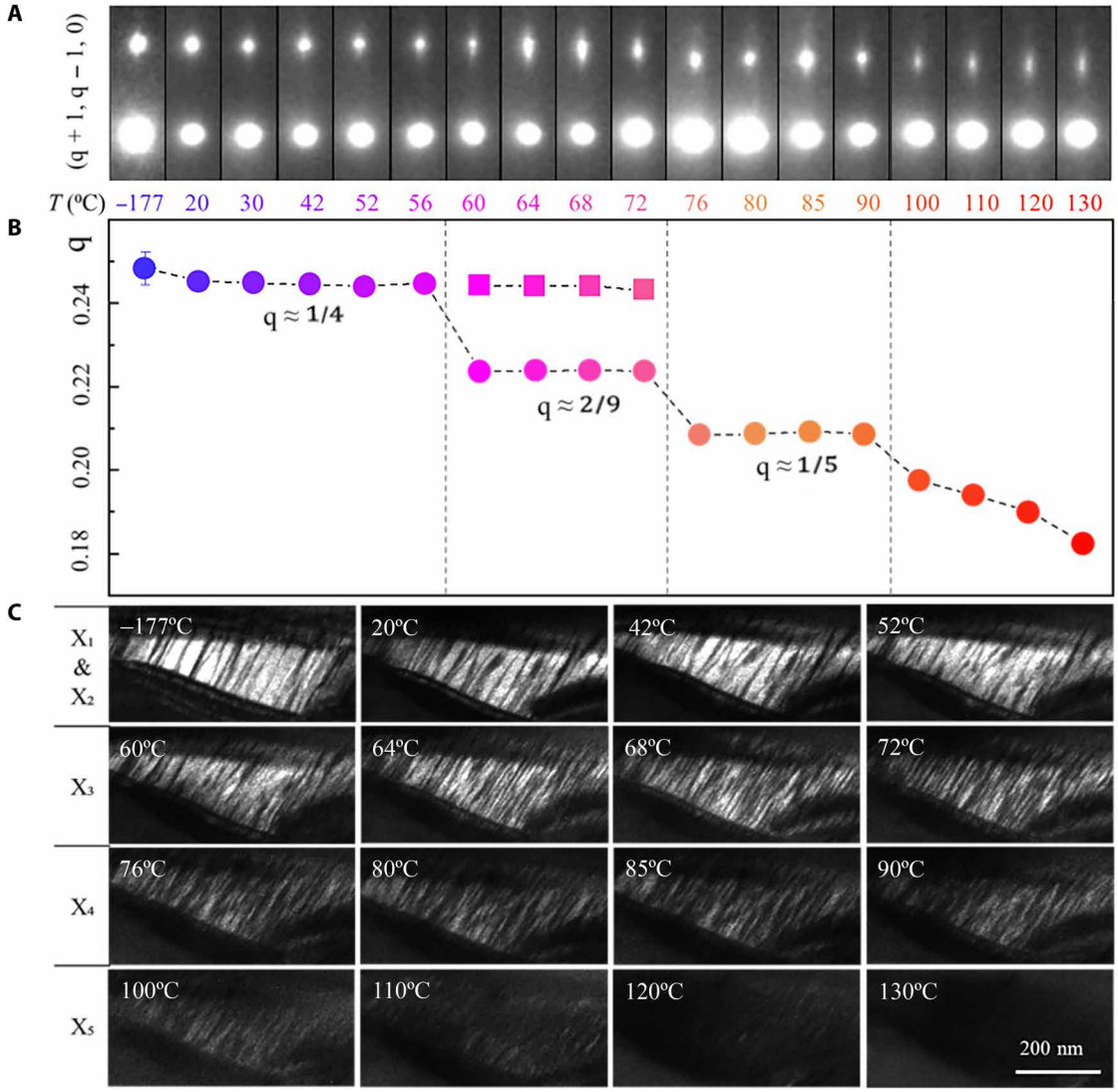

Fig. 2. The transition behavior of modulated structure. (**A** and **C**) Temperature dependence of SAED patterns and corresponding dark-field images, respectively. (**B**) The modulation wave vector as function of the temperature.

than continuously changes, from subregions X_2 to X_3 and then to subregion X_4. The subregion X_5, where satellite reflection approaches the main reflection, is an exception because it connects the region of paraelectric phase. Second, the $\mathbf{q} \approx 1/4$ and 2/9 phases are found to coexist in subregion X_3, which, along with simultaneously increased density of parallel interfacial defects (Fig. 2C) as will be described later, may form some one-dimensional disorder and contribute to the diffuse and streaked reflections. The corresponding intensity profiles of satellite reflections in fig. S4 show that the relative content of $\mathbf{q} \approx 1/4$ and $\mathbf{q} \approx 2/9$ phases can be affected by temperature. This implies that these modulated phases are close in energy and compete with each other.

By plotting the modulation wave vector as function of temperature (Fig. 2B), the behavior of PPT among AFE phases can be more clearly accessed. Obviously, the most notable feature is phase locking in step-like fashion, which indeed exhibit a DS feature, where, in principle, an infinite number of commensurate modulated phases can be expected by tuning the extrinsic parameters. The DS in magnetic system can be described by the simple axial next-nearest-neighbor Ising (ANNNI) model. In analogy, it is believed that the competition between the FE nearest-neighbor interaction and the AFE next-nearest-neighbor interaction are responsible for the given various orderings of electric dipoles.

The evolution of real-space microstructure in the process of DS transition is presented in Fig. 2C. It can be seen that the ground AFE state is characterized by a series of nearly parallel interfacial defects. For the transition from X_1 to X_2, the microstructure has barely changed because they have the same modulation wave vector ($\mathbf{q} \approx 1/4$). During transition from X_2 to X_3 (see 60° and 64°C), the new $\mathbf{q} \approx 2/9$ phase emerges accompanied by proliferation of interfacial defects, which initiates from the right part of the observing area. Thus, different electric dipole ordering phases coexist in a single domain with spatial separation on nanoscale. As the temperature continues to increase (see 68° and 72°C), the density of interfacial defects increases sharply because the $\mathbf{q} \approx 2/9$ phase becomes dominant. For the $\mathbf{q} \approx 1/5$ phase in subregion X_4 (see 76° to 90°C), on the other hand, high-density interfacial defects maintain but are shorter than the ones in $\mathbf{q} \approx 2/9$ phase. Further increasing temperature into subregion X_5, the contract of interfacial defects continues to decrease and lastly disappear as the modulated phase transforms to the paraelectric phase.

Previous works have demonstrated that it is the atomic position that exhibits one-dimensional sinusoidal modulation in $PbZrO_3$-based AFE materials (*15*, *26*). In this case, the modulated structure $s_m(\mathbf{r})$, as illustrated in Fig. 3A, can be described as the combination of a basic structure $s(\mathbf{r})$ and a modulation function $f(\mathbf{r})$ (*27*, *28*)

$$s_m(\mathbf{r}) = s(\mathbf{r}) + f(\mathbf{r})$$

where $s(\mathbf{r}) = k$, $0 \le k \le A$ and $f(\mathbf{r}) = A \sin(2\pi\mathbf{q}r + \varphi)$. The parameters k, A, $\mathbf{q}$, and φ refer to constant displacement, amplitude, modulation wave vector, and phase, respectively.

There are three basic states of matter (Fig. 3B) that can be derived from the following descriptions: (i) The modulated structure is FE state when the basic structure has a constant displacement and the modulation function is zero; (ii) the modulated structure is AFE state when the modulation function solely occurs with the basic structure having a zero displacement; (iii) the modulated structure is ferrielectric state with net polarization when the atomic displacement is contributed by both basic structure and modulation function. Thus, the competition between the FE nearest-neighbor interaction and the AFE next-nearest-neighbor interaction in ANNNI model can be considered as the interplay between basic structure and modulation function. The fact that the experimental observations always present ferrielectric configuration, in turn, suggests that the competing FE and AFE interaction does remain active.

By investigating the parameters k, A, $\mathbf{q}$, and φ in description of the modulated structure, we can easily understand the formation mechanism of the DS. The $\mathbf{q}$ determines the position of steps in DS, while the A, k, and φ give the specific electric dipole configuration. That is, when the $\mathbf{q}$ is fixed, various modulated phases can be achieved by tuning other parameters. This description is very similar with that of energy levels of electrons in atoms, i.e., principal quantum number characterizes the electron shell, while the angular quantum number characterizes the subshell and so on.

Figure 3 (C to E) shows the proposed configurations by changing A, $\mathbf{q}$, and/or φ for $\mathbf{q}$ = 1/4, 2/9, and 1/5 phases. It can be anticipated that a small perturbation will drive these isoperiodic phases to switch from one to another. For the $\mathbf{q}$ = 1/4 phases illustrated in Fig. 3C, we indeed observed similar configuration by atomic-scale imaging (fig. S5). Thus, a large number of nearly degenerate electric dipole ordering phase should occur in every isoperiodic step, which result in the appearance of the DS. Many long-range ordered configurations, especially for the $\mathbf{q}$ = 2/9 and 1/5 phases, have certain (110) planes with nearly zero displacement (see circles in Fig. 3, D and E). As a result, these modulated phases can be named as antiferroparaelectric phase, being analogous to antiferroparamagnetic phase, because their configuration contains paraelectric layers.

Because of the temperature induced by many isoperiodic phases in each step and the coexistence of modulated phases with different $\mathbf{q}$ values, a huge delay for the sharp structure change is expected, which will give rise to a good thermal stability of the property, such as energy storage density. From practical application viewpoint, X5R-type dielectric capacitors, where the energy storage density variation is below 15% in the temperature range of −55° to 85°C, have been the mainstay components in electronic devices, including mobile and medical devices where high energy density at medium applied electric field is required. Considering this, the unipolar *P-E* loops of PLZS ceramic (Fig. 4A) were measured at sequential temperatures within X5R temperature range for evaluation of the energy storage performance.

The energy storage density of the dielectric capacitors can be calculated through the *P-E* loops. $W_{tot} = \int_0^{P_{max}} E dP$, $W_{rec} = \int_{P_r}^{P_{max}} E dP$, and $\eta = W_{rec}/W_{tot}$ are the total energy storage density, recoverable energy storage density, and energy efficiency, respectively. The P_{max}, E_F, and E_A are the maximum polarization, forward switching field, and backward switching field. Figure 4 (B and C) shows P_{max}, E_F, E_A, W_{tot}, W_{rec}, and η determined from the *P-E* loops as a function of temperature. It can be seen that P_{max} and E_A/E_F show mild variations but opposite trend, with values being in the range of 38.1 to 41.8 μC/cm^2 and 282 to 209 kV/cm/253 to 202 kV/cm, respectively, which lead to the W_{tot} (9.5 to 7.6 J/cm^3)/ W_{rec} (8.0 to 6.5 J/cm^3), exhibiting good thermal stability to meet the X5R requirements. Meanwhile, the η remains a high value of ≥83% over the X5R temperature range.

Despite many significant progresses have been recently achieved in obtaining high energy storage density for bulk ceramics, further

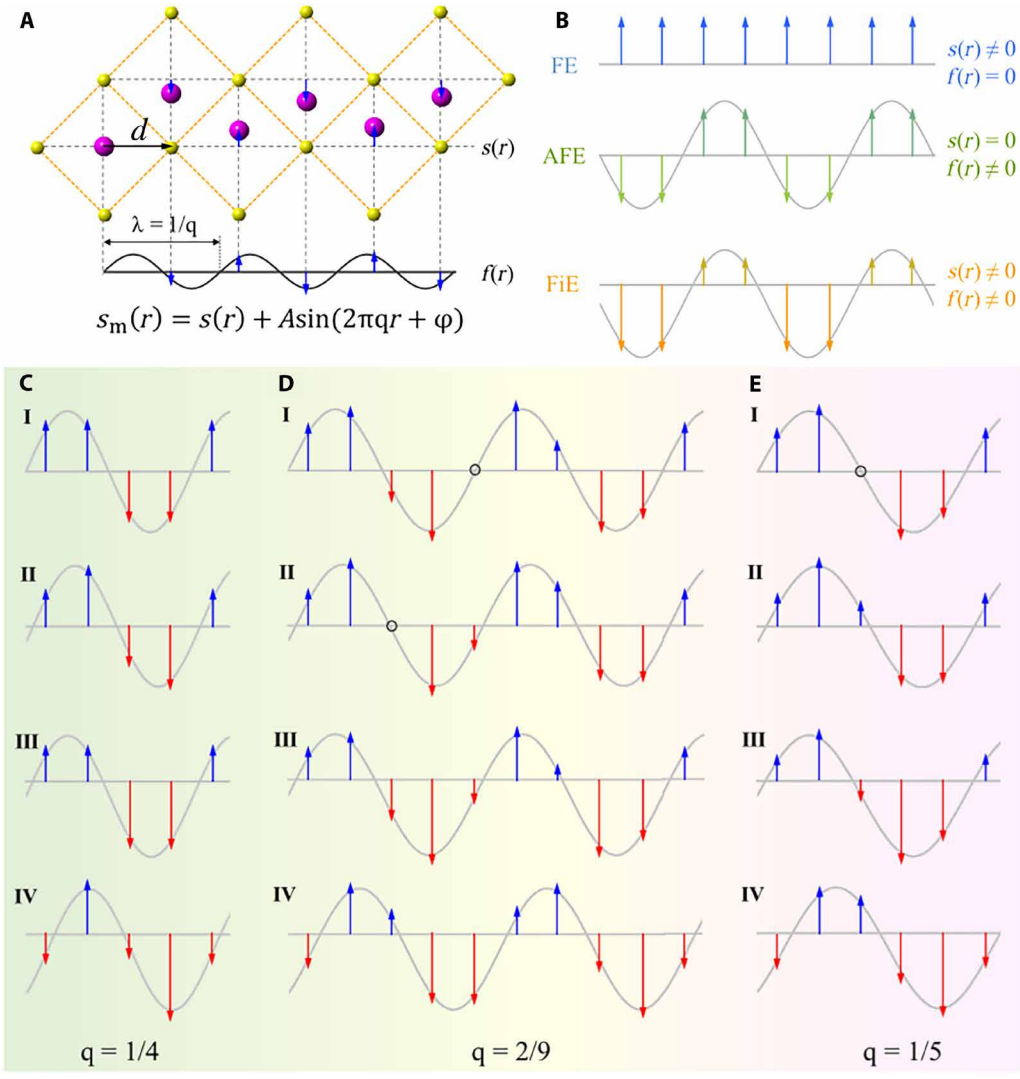

Fig. 3. Mathematical description of electric dipole configuration. (**A**) A schematic diagram elucidating the one-dimensional displacive modulation in perovskite structure, where oxygen anions are left out for the sake of simplicity. The A-site and B-site cations are colored by purple and yellow, respectively. The combination of the basic structure $s(r)$ with periodicity d, sinusoidal modulation wave with amplitude A, modulation wave vector **q**, and phase position φ gives the modulated structure $s_m(r)$. (**B**) Three basic states of matter derived from the modulated structure $s_m(r)$. FiE, ferrielectric. (**C** to **E**) Proposed configurations by tuning A, **q**, and/or φ for **q** = 1/4, 2/9, and 1/5 phases, respectively.

efforts should be used to improve the thermal stability for practical application. Figure 4D summarizes recent studies with considering thermal stability for representative lead-free and lead-based ceramics (including bulk ceramics and multilayer ceramic capacitors, see detailed compositions in table S1) (*29*–*40*). It can be seen that, at room temperature, the highest W_{rec} = 7.7 J/cm^3 was achieved at a medium electric field of 310 kV/cm for PLZS, which is superior to all other systems. By further increasing the applied electric field, the W_{rec} can reach a very high value of 9.4 J/cm^3 (fig. S6). Figure 4E gives the temperature-dependent energy storage density following the X5R standard, where the PLZS ceramic exhibits obviously superior energy storage performance than the reported bulk ceramics; meanwhile, the room temperature W_{rec} is more than twice that of the BT-based ceramics (7.7 J/cm^3 versus 3.0 J/cm^3), indicating that the PLZS ceramic is a promising candidate as X5R capacitor for device miniaturization.

In summary, our findings demonstrate the electric DS by investigating the temperature-induced phase transitions in PLZS ceramic. There are two essential elements for observing electric DS: One is ground AFE state and the other is PPT among AFE phase. The electric DS is similar to the magnetic DS in famous CeSb, and the mechanism underlying the phase locking strengthens the analogy between magnetic and electric, i.e., the competition between ferromagnetic/electric nearest-neighbor interaction and the antiferromagnetic/electric next-nearest-neighbor interaction. Thus, our results provide a broader category of phenomena involving interaction of the competing FE and AFE in the materials for future exploration of the electric DS. Moreover, the large number of

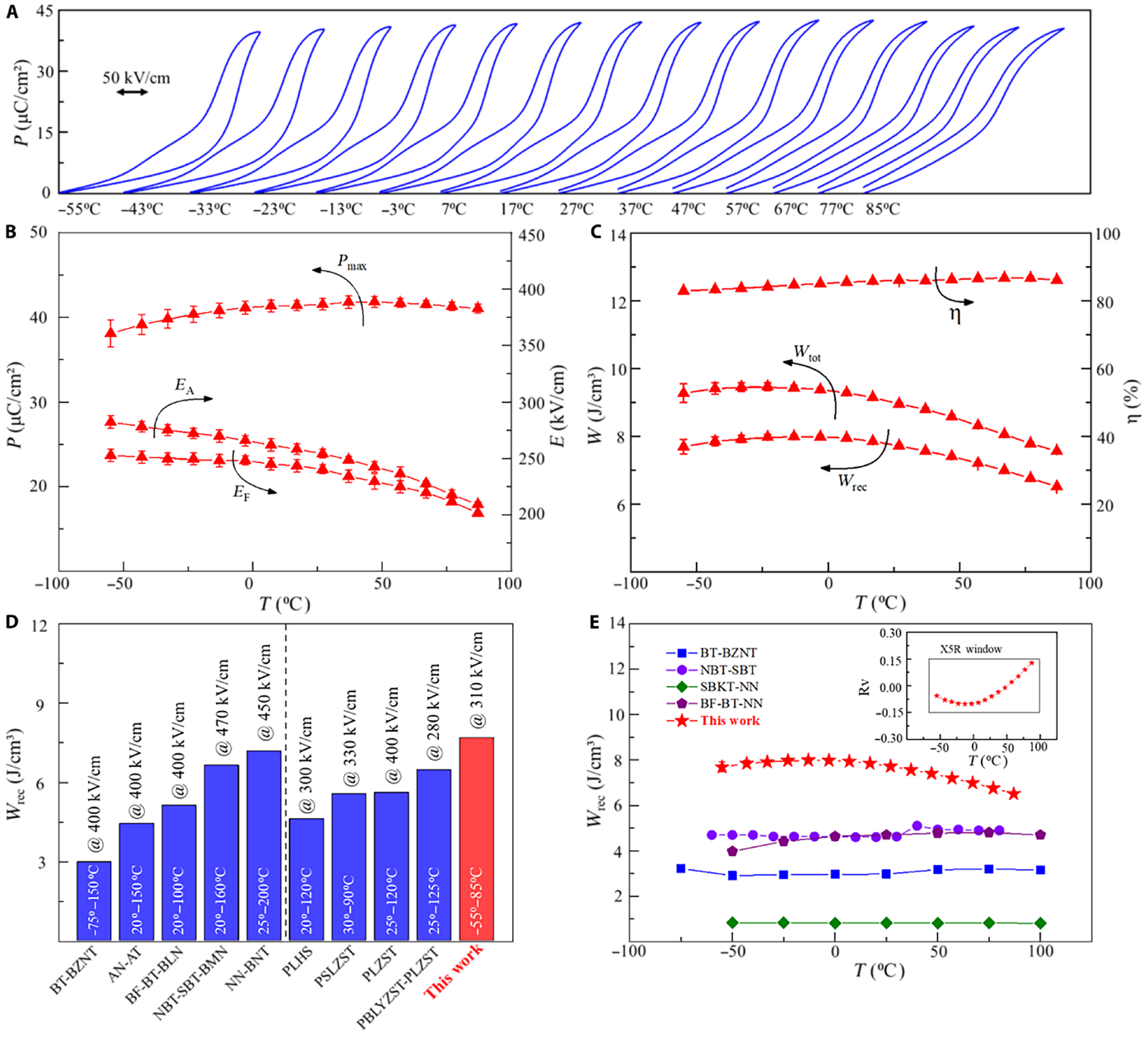

Fig. 4. DS enabled practical energy storage performance. (**A**) Evolution of hysteresis loops under 310 kV/cm as a function of temperature. (**B** and **C**) Energy storage characteristics (P_{max}, E_A, E_F, W_{tot}, W_{rec}, and η) as a function of temperature. (**D**) Comparison W_{rec} at room temperature for various representative bulk ceramics in previous researches that also took account into thermal stability. (**E**) Comparison of energy storage performance under X5R requirement.

degenerate modulated phases in DS leads to good temperature stability, which provides new pathway to optimize the comprehensive energy storage performance.

MATERIALS AND METHODS

Materials synthesis

PLZS ceramics were obtained by traditional high-temperature solid-phase sintering method. The raw materials for sintering PLZS are Pb_3O_4, La_2O_3, ZrO_2, and SnO_2 powders with purity higher than 99.0%. Because Pb volatilizes during sintering, a small amount of excess PbO [0.5 weight % (wt%)] was added. The preparation process of PLZS is as follows: First, the raw material powders were mixed and ball-milled for 6 hours, dried at 120°C, and then calcined at 900°C for 2 hours. The obtained PLZS powders were ball-milled again for 24 hours, dried at 120°C, mixed with 6 wt % polyvinyl acetate as a binder, and then pressed into disks with a diameter of 13 mm at 150 MPa. Last, the binder was burned out at 800°C for 2 hours, and the disks were sintered at 1300°C for 2 hours.

Dielectric measurements

The samples were polished to the thickness of 1 mm and silver electrode with diameter of 8 mm was used. The dielectric properties were measured at 1 kHz in the temperature range from −120° to

350°C with a broad dielectric Novocontrol Alpha spectrometer (Novocontrol Technologies, Montabaur, Germany).

Electric property characterization

The samples were polished to the thickness of 0.15 mm, and the silver films were sprayed with a diameter of 0.75 mm on the surface as electrode. The unipolar polarization-electric field (*P-E*) hysteresis loops at various temperatures were measured by aix ACCT TF 2000 analyzer FE measurement system (aixACCT Co., Aachen, Germany) at 10 Hz over a temperature range of −75° to 127°C.

Transmission electron microscopy

The transmission electron microscopy (TEM) specimens were prepared from ceramics by mechanical thinning, polishing, Ar^+ ion milling in a Gatan PIPS II, and then spraying carbon films with a thickness of 3 nm. To decrease ion beam damage during ion milling, the ion beam voltage was gradually degraded from 3 to 0.5 keV. In situ TEM experiments were carried out on heating holder that was controlled by a SmartSet Hot Stage controller (Gatan Model 901) and cryo-holder that was controlled by a temperature controller (Gatan Model 636), using JEOL JEM-2100F microscope that was operated at 200 kV. The SAED patterns and dark-field images at various temperatures were recorded with a charge-coupled device camera. The atomic-scale high-angle annular dark-field images were obtained on Cs-corrected JEOL JEM-ARM300F with probe size in 7C mode, convergence semiangle of 18 mrad and collection semiangle of 53 to 180 mrad. The atomic positions were extracted by MATLAB code (*41*, *42*). It should be noted that Pb can be precipitated from the sample that leads to formation of Pb vacancies if the temperature is over high or electron beam is overintense (fig. S7A). Being aware of this, the maximum temperature during in situ TEM was only up to 350°C, and the electron beam is spread to just cover the fluorescent screen in our experiment. By comparing the morphology and diffraction before and after heating (fig. S7B), it is found that the sample keeps clean when cooled, and there is almost no change in modulation period, implying that the formation of Pb vacancies was insignificant and thus had negligible impact on antipolar coupling during the experiment.

SUPPLEMENTARY MATERIALS

Supplementary material for this article is available at https://science.org/doi/10.1126/sciadv.abl9088

REFERENCES AND NOTES

1. A. K. Yadav, C. T. Nelson, S. L. Hsu, Z. Hong, J. D. Clarkson, C. M. Schlepütz, A. R. Damodaran, P. Shafer, E. Arenholz, L. R. Dedon, D. Chen, A. Vishwanath, A. M. Minor, L. Q. Chen, J. F. Scott, L. W. Martin, R. Ramesh, Observation of polar vortices in oxide superlattices. *Nature* **530**, 198–201 (2016).
2. S. Das, Y. L. Tang, Z. Hong, M. A. P. Gonçalves, M. R. McCarter, C. Klewe, K. X. Nguyen, F. Gómez-Ortiz, P. Shafer, E. Arenholz, V. A. Stoica, S.-L. Hsu, B. Wang, C. Ophus, J. F. Liu, C. T. Nelson, S. Saremil, B. Prasad, A. B. Mei, D. G. Schlom, J. Íñiguez, P. García-Fernández, D. A. Muller, L. Q. Chen, J. Junquera, L. W. Martin, R. Ramesh, Observation of room-temperature polar skyrmions. *Nature* **568**, 368–372 (2019).
3. D. D. Khalyavin, R. D. Johnson, F. Orlandi, P. G. Radaelli, P. Manuel, A. A. Belik, Emergent helical texture of electric dipoles. *Science* **369**, 680–684 (2020).
4. L. F. Lin, Y. Zhang, A. Moreo, E. Dagotto, S. Dong, Frustrated dipole order induces noncollinear proper ferrielectricity in two dimensions. *Phys. Rev. Lett.* **123**, 067601 (2019).
5. H. J. Zhao, P. Chen, S. Prosandeev, S. Artyukhin, L. Bellaiche, Dzyaloshinskii-Moriya-like interaction in ferroelectrics and antiferroelectrics. *Nat. Mater.* **20**, 341–345 (2021).
6. T. Matsuda, S. Partzsch, T. Tsuyama, E. Schierle, E. Weschke, J. Geck, T. Saito, S. Ishiwata, Y. Tokura, H. Wadati, Observation of a devil's staircase in the novel spin-valve system $SrCo_6O_{11}$. *Phys. Rev. Lett.* **114**, 236403 (2015).
7. K. Kuroda, Y. Arai, N. Rezaei, S. Kunisada, S. Sakuragi, M. Alaei, Y. Kinoshita, C. Bareille, R. Noguchi, M. Nakayama, S. Akebi, M. Sakano, K. Kawaguchi, M. Arita, S. Ideta, K. Tanaka, H. Kitazawa, K. Okazaki, M. Tokunaga, Y. Haga, S. Shin, H. S. Suzuki, R. Arita, T. Kondo, Devil's staircase transition of the electronic structures in CeSb. *Nat. Commun.* **11**, 2888 (2020).
8. K. Iwasa, Y. Arakaki, M. Kohgi, T. Suzuki, Evidence for crystal-lattice modulation due to spatially restricted enhancement of mixing effect in the low-carrier system CeSb. *J. Phys. Soc. Jpn.* **68**, 2498–2501 (2000).
9. J. V. Boehm, P. Bak, Devil's stairs and the commensurate-commensurate transitions in CeSb. *Phys. Rev. Lett.* **42**, 122–125 (1979).
10. B. Coqblin, Rare earths and actinides. *J. Magn. Magn. Mater.* , 1–19 (1982).
11. P. Fischer, G. Meier, B. Lebech, B. D. Rainford, O. Vogt, Magnetic phase transitions of CeSb. I. Zero applied magnetic field. *J. Phys. C Solid State Phys.* **11**, 345–364 (1978).
12. M. E. Fisher, W. Selke, Infinitely many commensurate phases in a simple ising model. *Phys. Rev. Lett.* **44**, 1502–1505 (1980).
13. P. Bak, Commensurate phases, incommensurate phases and the devil's staircase. *Rep. Prog. Phys.* **45**, 587–629 (1982).
14. Y. Yamada, N. Hamaya, A unified view of incommensurate-commensurate phase transitions in A_2BX_4 type crystals. *J. Phys. Soc. Jpn.* **52**, 3466–3474 (1983).
15. T. Ma, Z. Fan, B. Xu, T. H. Kim, P. Lu, L. Bellaiche, M. J. Kramer, X. Tan, L. Zhou, Uncompensated polarization in incommensurate modulations of perovskite antiferroelectrics. *Phys. Rev. Lett.* **123**, 217602 (2019).
16. Z. Fu, X. Chen, Z. Li, T. Hu, L. Zhang, P. Lu, S. Zhang, G. Wang, X. Dong, F. Xu, Unveiling the ferrielectric nature of $PbZrO_3$-based antiferroelectric materials. *Nat. Commun.* **11**, 3809 (2020).
17. Z. Xu, D. Viehland, P. Yang, D. A. Payne, Hot-stage transmission electron microscopy studies of phase transformations in tin-modified lead zirconate titanate. *J. Appl. Phys.* **74**, 3406–3413 (1993).
18. D. Viehland, D. Forst, J. Li, Compositional heterogeneity and the origins of the multicell cubic state in Sn-doped lead zirconate titanate ceramics. *J. Appl. Phys.* **75**, 4137–4143 (1994).
19. W. H. Chan, Z. Xu, T. F. Hung, H. Chen, Effect of La substitution on phase transitions in lead zirconate stannate titanate (55/35/10) ceramics. *J. Appl. Phys.* **96**, 6606–6610 (2004).
20. M. Deluca, Z. G. Al-Jlaihawi, K. Reichmann, A. M. T. Bell, A. Feteira, Remarkable impact of low $BiYbO_3$ doping levels on the local structure and phase transitions of $BaTiO_3$. *J. Mater. Chem. A* **6**, 5443–5451 (2018).
21. D. Viehland, D. Forst, Z. Xu, J. F. Li, Incommensurately modulated polar structures in antiferroelectric Sn-modified lead zirconate titanate: The modulated structure and its influences on electrically induced polarizations and strains. *J. Am. Ceram. Soc.* **78**, 2101–2112 (1995).
22. D. Viehland, Transmission electron microscopy study of high-Zr-content lead zirconate titanate. *Phys. Rev. B.* **52**, 778 (1995).
23. D. I. Woodward, I. M. Reaney, Electron diffraction of tilted perovskites. *Acta Crystallogr. B* **61**, 387–399 (2005).
24. I. M. Reaney, D. I. Woodward, C. A. Randall, Displacive phase transitions and intermediate structures in perovskites. *J. Am. Ceram. Soc.* **94**, 2242–2247 (2011).
25. J. Rossat-Mignod, P. Burlet, H. Bartholin, O. Vogt, R. Lagnier, Specific heat analysis of the magnetic phase diagram of CeSb. *J. Phys. C Solid State Phys.* **13**, 6381–6389 (1980).
26. E. Sawaguchi, H. Maniwa, S. Hoshino, Antiferroelectric structure of lead zirconate. *Phys. Rev.* **83**, 1078–1078 (1951).
27. W. Steurer, T. Haibach, Reciprocal-space images of aperiodic crystals, in *International Tables for Crystallography*, U. Shmueli, Ed. (KAP, 2006), vol. B, chap. 4.6.
28. S. V. Smaalen, Superstructures and the commensurate approximation, in *Incommensurate Crystallography* (OUP, ed. 1, 2007), pp. 113–124.
29. P. Zhao, H. Wang, L. Wu, L. Chen, Z. Cai, L. Li, X. Wang, High-performance relaxor ferroelectric materials for energy storage applications. *Adv. Energy Mater.* **9**, 1803048 (2019).
30. N. Luo, K. Han, M. J. Cabral, X. Liao, S. Zhang, C. Liao, G. Zhang, X. Chen, Q. Feng, J. F. Li, Y. Wei, Constructing phase boundary in $AgNbO_3$ antiferroelectrics: Pathway simultaneously achieving high energy density and efficiency. *Nat. Commun.* **11**, 4824 (2020).
31. G. Wang, Z. Lu, H. Yang, H. Ji, A. Mostaed, L. Li, Y. Wei, A. Feteira, S. Sun, D. C. Sinclair, D. Wang, I. M. Reaney, Fatigue resistant lead-free multilayer ceramic capacitors with ultrahigh energy density. *J. Mater. Chem. A* **8**, 11414–11423 (2020).
32. H. Ji, D. Wang, W. Bao, Z. Lu, G. Wang, H. Yang, A. Mostaed, L. Li, A. Feteira, S. Sun, F. Xu, D. Li, C. Ma, S. Liu, I. M. Reaney, Ultrahigh energy density in short-range tilted NBT-based lead-free multilayer ceramic capacitors by nanodomain percolation. *Energy Stor. Mater.* **38**, 113–120 (2021).
33. H. Qi, R. Zuo, A. Xie, A. Tian, J. Fu, Y. Zhang, S. Zhang, Ultrahigh energy-storage density in $NaNbO_3$-based lead-free relaxor antiferroelectric ceramics with nanoscale domains. *Adv. Funct. Mater.* **29**, 1903877 (2019).
34. W. Chao, T. Yang, Y. Li, Achieving high energy efficiency and energy density in $PbHfO_3$-based antiferroelectric ceramics. *J. Mater. Chem. C.* **8**, 17016–17024 (2020).

35. Q. Zhang, H. Tong, J. Chen, Y. Lu, T. Yang, X. Yao, Y. He, High recoverable energy density over a wide temperature range in Sr modified (Pb,La)(Zr,Sn,Ti)O_3 antiferroelectric ceramics with an orthorhombic phase. *Appl. Phys. Lett.* **109**, 262901 (2016).
36. S. Chen, X. Wang, T. Yang, J. Wang, Composition-dependent dielectric properties and energy storage performance of (Pb,La)(Zr,Sn,Ti)O_3 antiferroelectric ceramics. *J. Electroceram.* **32**, 307–310 (2014).
37. J. Yi, L. Zhang, B. Xie, S. Jiang, The influence of temperature induced phase transition on the energy storage density of anti-ferroelectric ceramics. *J. Appl. Phys.* **118**, 124107 (2015).
38. J. Li, F. Li, Z. Xu, S. Zhang, Multilayer lead-free ceramic capacitors with ultrahigh energy density and efficiency. *Adv. Mater.* **30**, e1802155 (2018).
39. P. Zhao, Z. Fang, X. Zhang, J. Chen, Y. Shen, X. Zhang, Q. An, C. Yang, X. Gao, S. Zhang, B. Tang, Aliovalent doping engineering for A- and B-sites with multiple regulatory mechanisms: A strategy to improve energy storage properties of $Sr_{0.7}Bi_{0.2}TiO_3$-based lead-free relaxor ferroelectric ceramics. *ACS. Appl. Mater. Inter.* **13**, 24833–24855 (2021).
40. H. Qi, A. Xie, A. Tian, R. Zuo, Superior energy-storage capacitors with simultaneously giant energy density and efficiency using nanodomain engineered $BiFeO_3$-$BaTiO_3$-$NaNbO_3$ lead-free bulk ferroelectrics. *Adv. Energy. Mater.* **10**, 1903338 (2019).
41. A. De Backer, K. H. W. van den Bos, W. Van den Broek, J. Sijbers, S. Van Aert, StatSTEM: An efficient approach for accurate and precise model-based quantification of atomic resolution electron microscopy images. *Ultramicroscopy* **171**, 104–116 (2016).
42. S. Van Aert, A. De Backer, G. T. Martinez, A. J. den Dekker, D. Van Dyck, S. Bals, G. Van Tendeloo, Advanced electron crystallography through model-based imaging. *IUCrJ* **3**, 71–83 (2016).

Acknowledgments: We acknowledge discussions with C.-G. Duan and J. Liu. **Funding:** This work is supported by the National Natural Science Foundation of China (grant nos. 52002388 and U2002217), Shanghai Science and Techonology Innovation Acition Plan (21ZR1472400), and Shanghai technical platform for testing and characterization on inorganic materials (19DZ2290700). **Author contributions:** Z.L., Z.F., X.C., and F.X. conceived the experiments. X.C., H.C., and Y.L. synthesized the samples and measured macroscopic properties. Z.L., Z.F., T.H., Z.Y., L.Z., and H.Y. performed the TEM experiments. Z.L., Z.F., S.Z., G.W., X.D., and F.X. analyzed the data, wrote, and edited the manuscript. All authors contributed to the discussion and manuscript preparation. **Competing interests:** The authors declare that they have no competing interests. **Data and materials availability:** All data needed to evaluate the conclusions in the paper are present in the paper and/or the Supplementary Materials.

Submitted 13 August 2021
Accepted 14 February 2022
Published 6 April 2022
10.1126/sciadv.abl9088